Resonant dynamics of three-dimensional skyrmionic textures in thin film multilayers

Titiksha Srivastava, Yanis Sassi, Fernando Ajejas, Aymeric Vecchiola, Igor Ngouagnia, Herve Hurdequint, Karim Bouzehouane, Nicolas Reyren, Vincent Cros, Thibaut Devolder, et al.

Resonant dynamics of three-dimensional skyrmionic textures in thin film multilayers

Cite as: APL Mater. 11, 061110 (2023); doi: 10.1063/5.0150265
Submitted: 13 March 2023 • Accepted: 9 May 2023 •
Published Online: 1 June 2023

Titiksha Srivastava,[1,2,3,a] Yanis Sassi,[1] Fernando Ajejas,[1] Aymeric Vecchiola,[1] Igor Ngouagnia Yemeli,[2] Hervé Hurdequint,[2] Karim Bouzehouane,[1] Nicolas Reyren,[1] Vincent Cros,[1] Thibaut Devolder,[3] Joo-Von Kim,[3,b] and Grégoire de Loubens[2,c]

AFFILIATIONS

[1] Unité Mixte de Physique, CNRS, Thales, Université Paris-Saclay, 91767 Palaiseau, France
[2] SPEC, CEA, CNRS, Université Paris-Saclay, 91191 Gif-sur-Yvette, France
[3] Centre de Nanosciences et de Nanotechnologies, CNRS, Université Paris-Saclay, 91120 Palaiseau, France

[a] Electronic mail: titiksha.srivastava@c2n.upsaclay.fr
[b] Author to whom correspondence should be addressed: joo-von.kim@c2n.upsaclay.fr
[c] Electronic mail: gregoire.deloubens@cea.fr

ABSTRACT

Skyrmions are topological magnetic solitons that exhibit a rich variety of dynamics, such as breathing and gyration, which can involve collective behavior in arrangements like skyrmion lattices. However, such localized excitations typically lie in the gap of the spin wave spectrum and do not couple to propagating modes. By combining magnetic force microscopy, broadband ferromagnetic resonance, and micromagnetics simulations, we show that in thin-film multilayers of $[Pt/FeCoB/AlO_x]_{20}$ a high-frequency (>12 GHz) mode accompanies the skyrmion lattice phase, which involves the coherent precession of the skyrmion cores that results in the generation of 50–80 nm wavelength spin waves flowing into the uniformly magnetized background. This observation is made possible by a Gilbert damping constant of ~0.02, which is nearly an order of magnitude lower than in similar ultrathin materials. The simulations also reveal a complex three-dimensional spin structure of the skyrmion cores, which plays a key role for spin wave generation.

I. INTRODUCTION

The dynamic response of magnetic materials at microwave frequencies represents a rich field of research for its fundamental interest and applications in information processing. Linear excitations in the form of spin waves (SWs) underpin the field of magnonics, which describes the paradigm of transmitting and processing information with such waves.[1–3] SW-based devices may allow for fast and energy-efficient logic applications,[4] and a growing number of proposals have shown potential uses for computing[5] and spectral analysis[6] by SW interference. Magnonic circuit elements, such as transistors,[7] diodes,[8] and filters,[9] have also been demonstrated in experiments based on the manipulation of dipole-dominated SWs with micrometer wavelengths. The generation and detection of shorter wavelength SWs, a prerequisite for miniaturization, is challenging, owing to the limitations of nanoscale fabrication. Recent studies have shown that short wavelength emission can be achieved by broadband antennae,[10] grating effects,[11–13] and spin torques.[14]

In this light, nonuniform magnetic textures have been explored for generating and manipulating spin waves and generally offer an alternative route to expand the range of useful phenomena for applications.[15] Such textures can appear spontaneously at the micro- and nano-scale in magnetic materials as a result of the competing interactions, namely, exchange, dipolar, and anisotropy. Magnetic textures like bubbles,[16,17] stripes,[18–20] and vortices[21,22] have been shown to exhibit a rich diversity of magnetization dynamics. For example, it has been demonstrated that magnetic domain walls can serve as nanoscale waveguides,[23,24] while the cores of magnetic vortices can be used to generate omnidirectional dipole-exchange SWs with sub-100 nm wavelengths.[25,26]

Recently, topologically non-trivial chiral magnetic configurations called skyrmions have generated much interest owing to

their robust and particle-like nature.[27] They can be stabilized at room temperature in thin films[28,29] with perpendicular magnetic anisotropy (PMA) and interfacial Dzyaloshinskii–Moriya interaction (DMI), which provides different handles for tuning the desired magnetic parameters, both statically and dynamically.[30] On the one hand, their dc current-driven dynamics[31,32] could be exploited for racetrack memory and logic devices,[27] and on the other hand, their unique microwave response opens up the possibilities of skyrmion-based spin–torque oscillators,[33] rf detectors,[34] and reconfigurable magnonic crystals for microwave processing.[35–38] Skyrmions exhibit a rich variety of eigenmodes,[39–43] among which azimuthal bound states and breathing modes have been experimentally observed at low temperatures in bulk crystals,[44–46] which have low damping parameters. Only very recently, resonant dynamics with specific spectroscopic signatures of thin-film multilayers hosting skyrmions has been evidenced.[47,48] However, much remains to be explored and understood concerning their individual and collective resonant response to microwave excitations.

In this work, we report a study of the resonant dynamics of ultrathin film multilayers with perpendicular magnetic anisotropy, which host stable skyrmion lattices under ambient conditions with typical periods of 250 nm and skyrmion diameters of 100 nm, while exhibiting Gilbert damping in the range of $\alpha \simeq 0.02$. By combining magnetic force microscopy (MFM) and ferromagnetic resonance (FMR) experiments with micromagnetic simulations, we can identify distinct SW modes associated with the skyrmion lattice phase. At low frequency ($\lesssim$2 GHz), we observe a number of modes related to the precession of the uniform background state of individual layers close to or at the surfaces of the stack, along with eigenmodes localized to the skyrmion edges. At intermediate frequencies (2–8 GHz), the precession of the uniform background near the center of the stack dominates the response. Similar modes were previously described and reported in bulk crystals,[45,46] and lately in thin films.[47,48] Intriguingly, we also observe a well-defined mode at high frequency (>12 GHz), which corresponds to the in-phase precession of the magnetization within the skyrmion cores. The skyrmions here, have a distinct three-dimensional structure due to the competition between all the existing magnetic interactions in these multilayers, notably the interlayer dipolar effects.[49,50] Strikingly, this skyrmion core precession is accompanied by the emission of spin waves, with wavelengths in the range of 50 to 80 nm, into the uniformly magnetized background. These SWs interfere with those generated at neighboring skyrmion cores, yielding a collective dynamical state governed by the subtle interplay between the skyrmion diameter, the wavelength of the emitted SWs, and the skyrmion lattice periodicity.

II. RESULTS

A. Multilayer composition

The basic element of the multilayer film studied is the $Pt(1.6)/Fe_{0.7}Co_{0.1}B_{0.2}(1.2)/AlO_x(1.0)$ trilayer (hereafter referred to as $Pt/FeCoB/AlO_x$), where the figures in parentheses indicate the nominal film thickness in nm. This trilayer lacks inversion symmetry along the film thickness direction whereby the Dzyaloshinskii–Moriya interaction is promoted at the interfaces of the ferromagnetic FeCoB film with Pt (and possibly AlO_x[51]). The trilayer is repeated 20 times to form our multilayer sample (see Appendix A), as shown in Fig. 1(a). The choice of Fe-rich FeCoB and the aforementioned optimized thicknesses of Pt and FeCoB, along with the AlO_x interface, allow having sufficient DMI and PMA[52–55] to stabilize skyrmions, while limiting spin pumping effects that would otherwise lead to an increased damping coefficient.[56] We estimate by FMR a Gilbert damping constant of $\alpha = 0.022$ and an inhomogeneous broadening of ~18 mT (see Fig. 1 in the supplementary material) for our samples, which are relatively low for such multilayer systems.[47,56] The overall magnetic volume is enhanced with the 20 repetitions of the trilayer, which not only increases the thermal stability of the skyrmions[28] but also provides a larger signal-to-noise ratio for inductive measurements.

B. Static characterization

Figure 1(b) shows the out-of-plane hysteresis curve of the sample measured by alternating gradient field magnetometer, which is characteristic of thin films hosting skyrmions. The quasi-static magnetization configuration of the sample is probed by MFM using a low moment tip by sweeping the out-of-plane (OP) field from negative $(-z)$ to positive $(+z)$ saturation as illustrated in Fig. 1(d). On decreasing the field from negative saturation, we observe nucleation of skyrmions with an average diameter around 100 nm [zone (i)], which develops into a dense lattice structure upon further reduction of the field [zone (ii)]. In zone (iii) some of the skyrmions elongate and/or coalesce to form stripes leading to a mixture of skyrmions and stripe domains. At small positive fields, labyrinthine domains [zone (iv)] become energetically stable and, upon increasing the field further, lead to the formation of a dense skyrmion lattice once again [zone (vi)]. From the MFM images, we extract the density of skyrmions as a function of the applied field $\mu_0 H_z$ and apparent skyrmion diameter for the ranges of magnetic field where the skyrmion density is close to maximum, as shown in Fig. 1(c).

It is interesting to note that the observed skyrmion lattice is almost quasi-periodic hexagonal (see Fig. 2 in the supplementary material) whereas more amorphous states were observed in previous studies[47,48] in such kind of multilayered films, indicating only minor inhomogeneities and defects induced during the film growth in our samples. The skyrmion lattice phase is also remarkably stable at positive field, as shown by the constant skyrmion density of about 21 per square micron between 200 and 350 mT.

By using the period of the labyrinthine domain pattern in Fig. 1(d) (iv) and the measured values of saturation magnetization ($M_s = 1.2$ MA/m) and uniaxial anisotropy ($K_u = 0.7$ MJ/m^3), we estimate the DMI to be $D = 1.2$ mJ/m^2 with an exchange constant of $A = 15$ pJ/m for our sample (see Appendix B), which are in good agreement with direct experimental determination of these parameters in Pt/FeCoB/MgO stacks.[57]

C. Dynamic characterization

The resonant dynamics of the sample was probed by broadband FMR using a coplanar waveguide [Fig. 2(d)] and a vector network analyzer (VNA). The dc out-of-plane field is swept from negative to positive values while the frequency of the in-plane ac field is scanned over a range of 0.1–20 GHz for each dc field step. The real and the imaginary parts of the transmission signal S_{21} are recorded and processed to remove a background signal that is independent of the dc field, which improves the contrast (see Appendix A and Fig. 3 in

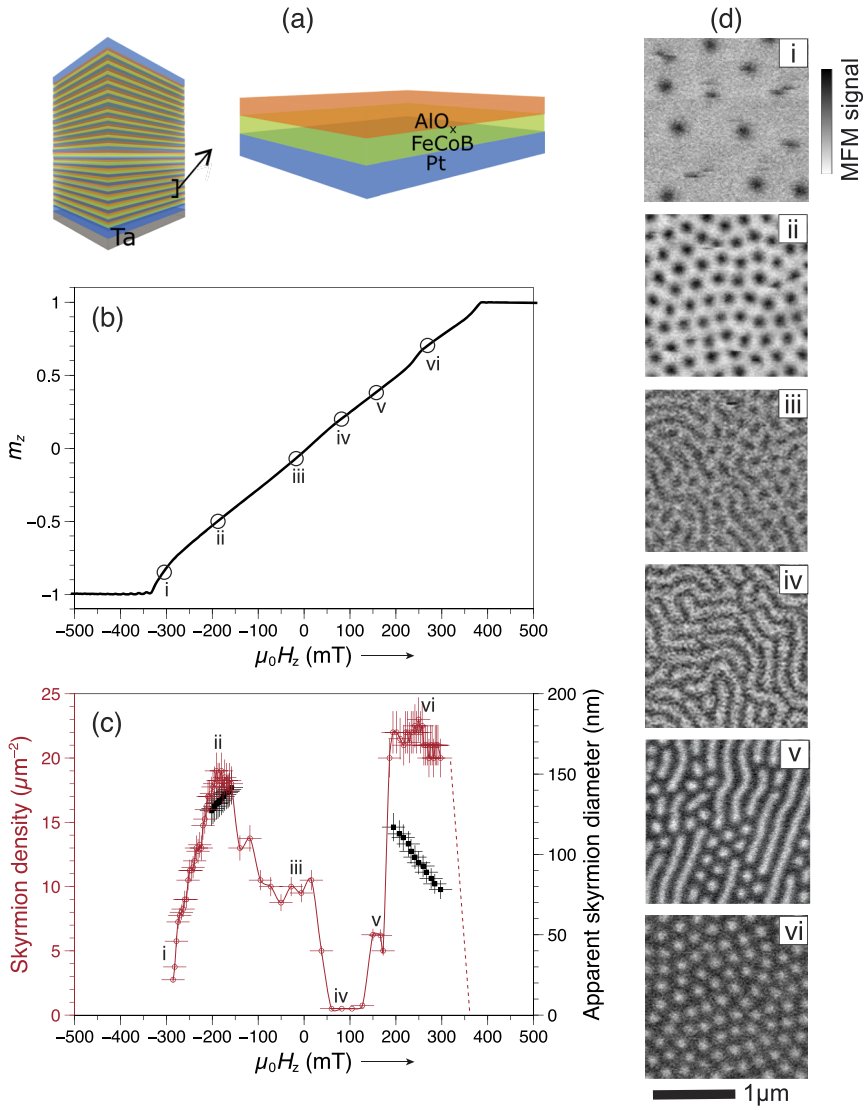

FIG. 1. Static characterization of the magnetic phases. (a) Schematics of the sample stack. (b) The out-of-plane (OP) magnetization curve on sweeping the field from negative to positive values. (c) The corresponding skyrmion density and apparent skyrmion diameter as a function of the field. The dashed red line indicates the possible extrapolation of the observed skyrmion density at higher positive field values in accordance with the OP hysteresis curve. The skyrmion diameter is extracted only for the field ranges where the skyrmion density is close to maximum (see Appendix C). (d) Magnetic domain configurations of the sample: (i) randomly distributed skyrmions, (ii) and (vi) skyrmion lattice, (iii) and (v) skyrmion–stripe mix, and (iv) labyrinthine domains, measured by MFM as a function of OP magnetic field [corresponding to the values marked in (b)] swept from negative to positive values.

the supplementary material). The corresponding frequency vs field map is shown in Fig. 2(a). In the saturated state, we observe the high intensity Kittel mode (KM) along with two additional low intensity secondary modes at higher field (see also Fig. 1 in the supplementary material). The latter are attributed to localized modes in the multilayer thickness that result from inhomogeneous interfacial couplings of our multilayer system.[58] In addition to the KM observed above saturation fields, three groups of modes with lower intensities appear when the magnetization enters a non-uniform state. On ramping the field from negative saturation toward zero, the KM softens close to $\mu_0 H_z = -335$ mT where skyrmions start to nucleate [see MFM images in Fig. 1(d)]. It then evolves into a mode with negative field dispersion (i.e., $\partial f/\partial|H_z| < 0$) as the skyrmion lattice grows denser, which we call the intermediate frequency mode (IFM). At this point, a weak amplitude mode also emerges at high frequency (>12 GHz) that has a positive field dispersion (i.e., $\partial f/\partial|H_z| > 0$) denoted as the high frequency mode (HFM). The IFM and HFM fade away close to zero field, where the static magnetization configuration consists of labyrinthine domains. While the IFM reappears as the field is increased toward positive values corresponding to a mixture of skyrmions and stripes, the HFM is visible only above 200 mT when the magnetization profile consists of a dense skyrmion lattice network [see Fig. 1(c)], and the IFM dispersion nearly flattens. We also notice that at the very same field a mode appears at low frequency (<2 GHz) followed by another at even lower frequencies, which we refer to as low frequency modes (LFM). The HFM mode fades away at fields when the skyrmion lattice transforms into isolated skyrmions. The IFM continues beyond this point, however, with an abrupt change of slope until the magnetization becomes uniform beyond 390 mT. The line cuts along fixed fields (−295 and 295 mT) and fixed frequencies (14 and 4 GHz) are shown in Figs. 2(b) and 2(c), respectively. The modes at negative and positive fields

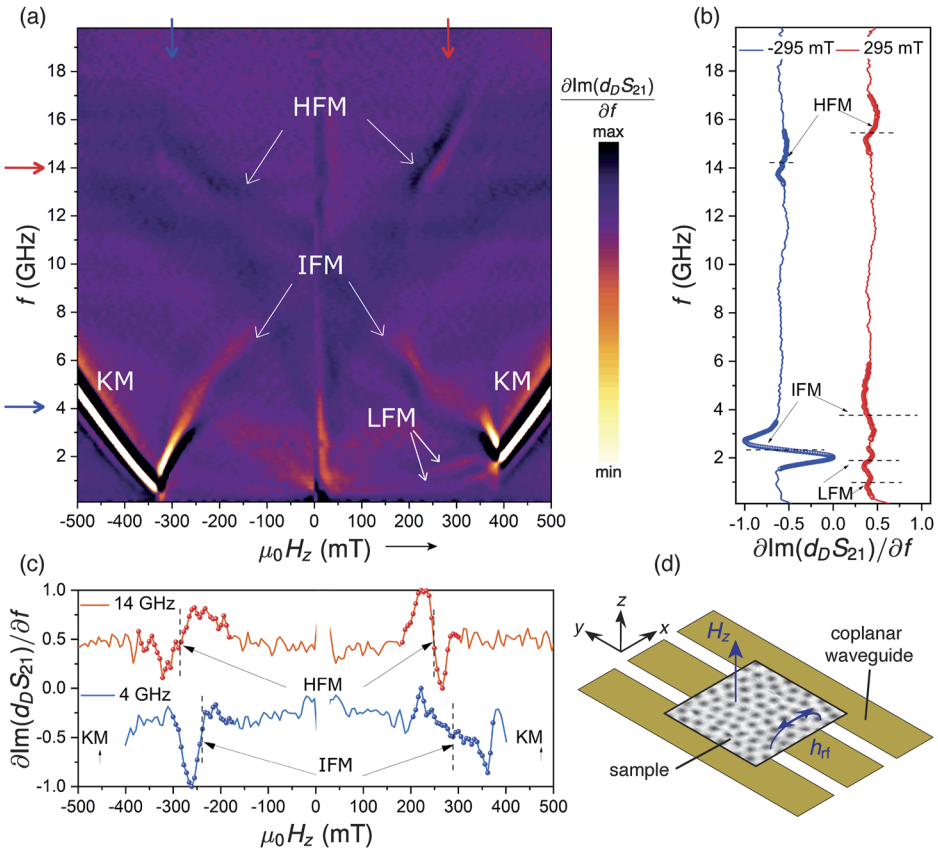

FIG. 2. Broadband ferromagnetic resonance. (a) Frequency-field dispersion map measured by VNA-FMR over a frequency range of 0.1 to 20 GHz with the applied OP field swept from −500 to 500 mT. Apart from the Kittel mode (KM) above saturation, several distinct modes appear in the non-saturated state which are labeled HFM: high frequency mode ($f > 12$ GHz), IFM: intermediate frequency mode ($f < 8$ GHz) and LFM: low frequency modes ($f < 2$ GHz). (b) Line cuts for fixed OP field values: −295 and 295 mT. (c) Line cuts for fixed frequency values: 4 and 14 GHz. (d) Schematic of the VNA-FMR setup.

are not symmetric but instead depend on the magnetic field history (see Fig. 4 in the supplementary material), as does the static magnetization profile.

D. Micromagnetic simulations

We performed simulations with the finite-difference micromagnetic code MUMAX3[59] in order to gain better insight into the static and dynamic properties of our sample (see Appendix D). We modeled the full 20-layer repetition of the Pt/FeCoB/AlO_x trilayer (with periodic boundary conditions in the film plane) in order to account for dipolar effects as accurately as possible, since it is known that the skyrmion core deviates from the usual tubular structure to complex three-dimensional configurations due to inhomogeneous dipolar fields along the multilayer thickness.[49] Figures 3(a) and 3(b) show the simulated hysteresis loop and the skyrmion density and apparent diameter variation as a function of the OP field swept from negative to positive values. The MFM images calculated from the simulated magnetization profiles (see Appendix C) are shown in Fig. 3(c). The field evolution of the simulated static characteristics presented in Figs. 3(a)–3(c) is found to be in good agreement with the experiments.

A striking feature of the labyrinthine domain and skyrmion structures found is that their micromagnetic configuration exhibits strong variations along the multilayer thickness direction. An example of such complex structures is shown in Fig. 3(d), where the m_z component is shown for a single skyrmion core in the lattice phase at $\mu_0 H_z = 285$ mT. The figure shows the contours for $m_z = 0.9$ (red), $m_z = 0$ (yellow), and $m_z = -0.9$ (blue) as surfaces where cubic interpolation has been used across the nonmagnetic layers. We note that the skyrmion core, in particular, the region of reversed magnetization $m_z \leq -0.9$, does not extend across the entire thickness of the multilayer. Recall that the FeCoB layers are only coupled together through dipolar interactions, which are sufficiently large to maintain an alignment of the core center but too weak to promote a coherent magnetization profile across the different layers. We can also observe that the magnetization in the uppermost layers at the core center is not reversed at all, but slightly tilted away from the film normal as indicated by the presence of the inverted cone. The in-plane components of the magnetic texture shown in Fig. 3(d) are presented in Fig. 3(e). Here, each cube represents the magnetic state of a finite-difference cell, where the color represents the orientation of the magnetization in the cell. In order to highlight the role of the in-plane components to complement the data shown in Fig. 3(d), the relative size and opacity of each cube is scaled with the function $1 - m_z^2$; this renders the regions of the uniform background and the reversed magnetization transparent. A clear skyrmion profile can be seen for the nine bottom layers, where the same left-handed (i.e., counterclockwise) Néel chirality is found in each layer. In layers 10 to 14, on the other hand, the in-plane component of the

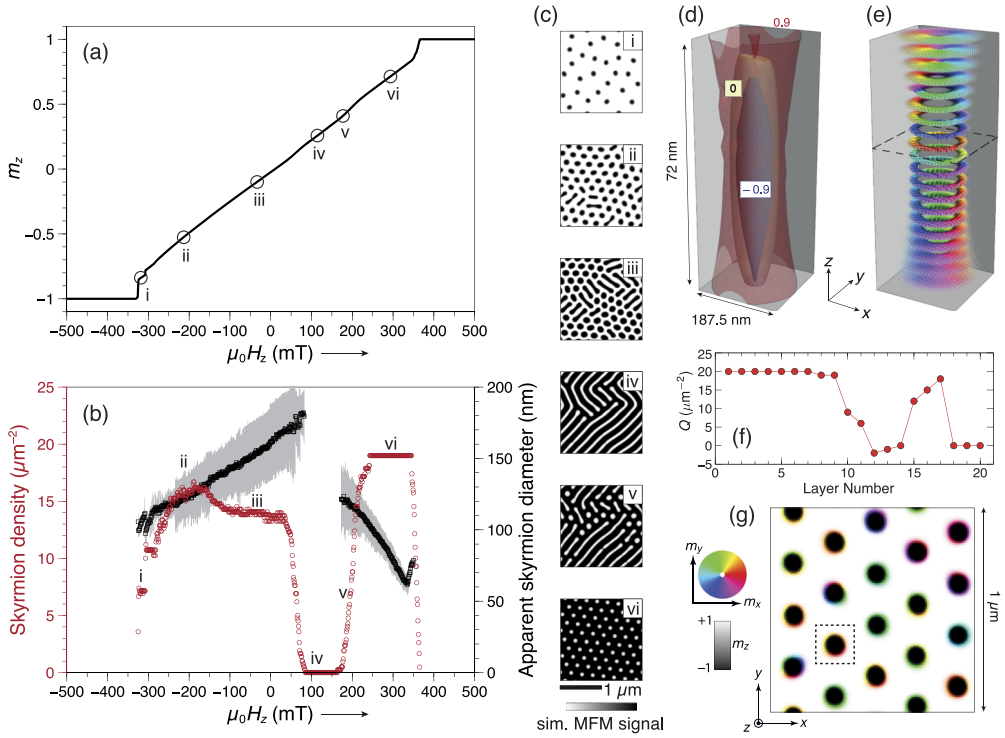

FIG. 3. Micromagnetic simulations of equilibrium magnetic configuration. (a) Simulated magnetization curve, (b) skyrmion density and diameter evolution, and (c) the corresponding simulated MFM images for the OP field swept from negative to positive values. The gray shaded area in (b) results from uncertainties in determining the skyrmion diameter, as discussed in Appendix C. (d) m_z contours and (e) in-plane components of the magnetization texture of a single skyrmion in the lattice phase at 285 mT. (f) Topological charge density Q per layer at 285 mT. (g) Magnetic configuration of layer 12 at 285 mT.

magnetization at the skyrmion boundary becomes more uniform and does not exhibit the same winding as in the bottom half of the stack. This means that the reversed domain structure is non-topological. A skyrmion profile reappears in layers 15, 16, and 17 but with a reversed chirality, where the in-plane magnetization components of the right-handed (i.e., clockwise) Néel structure are rotated by 180° in the plane with respect to their left-handed counterparts. Finally, in layers 18 to 20, we observe another type of non-topological texture where the core magnetization is closely aligned with the background magnetization, which corresponds to the inverted cone at the top of the stack in Fig. 3(d). Figure 3(f) shows the variation of the topological charge density per layer as a function of the layer number, which shows that a similar thickness dependence is observed across the skyrmion lattice. The skyrmions in the bottom half of the stack remain topological, while the top half comprises largely non-topological bubbles. Finally, Fig. 3(g) illustrates the magnetic configuration of layer 12 across the entire region simulated, where we can observe that the mainly uniformly magnetized regions of the magnetic bubble walls can vary greatly from one bubble to the next, with no discernible spatial order. We have verified that these features persist for finite difference cell sizes down to ~2 nm, which indicates that the complex magnetization structure does not arise from discretization effects (see Fig. 5 in the supplementary material). We note that similar three-dimensional textures have also been seen in Ta/CoFeB/MgO multilayers,[60] where topological spin configurations appear across the stack. The key difference with the system studied here is the stronger DMI, which competes with the dipolar interactions and leads to the variety of non-topological states observed.

We next discuss the dynamical response of the system, where the frequency-dependent susceptibility is computed under different applied fields as in Fig. 2(a) (see Appendix D). The simulated susceptibility map is shown in Fig. 4(a), which is determined from response of the static configurations computed in Fig. 3 to sinusoidal in-plane fields in the frequency range of 0.1 to 20 GHz. The Kittel mode (KM) is easily identified for the uniform state for fields above the saturation field. In the regime in which the magnetization is nonuniform, $-330 < \mu_0 H_z < 365$ mT, three distinct types of modes can be identified, as illustrated by the line cut at 285 mT shown in Fig. 4(b). As in experiments, the KM transforms into a negative field dispersion mode, an intermediate frequency mode (IFM), at fields where skyrmion nucleation begins. The IFM dispersion is rather rugged on the negative field side, where the skyrmion density rapidly evolves with field, and a faint splitting of IFM is seen around −260 mT. The IFM is asymmetric with respect to zero field and exhibits smoother variations on the positive field side. Similar to the negative field side, another branch of the IFM is seen for positive fields appearing at around 200 mT, which is relatively flat around 4 GHz

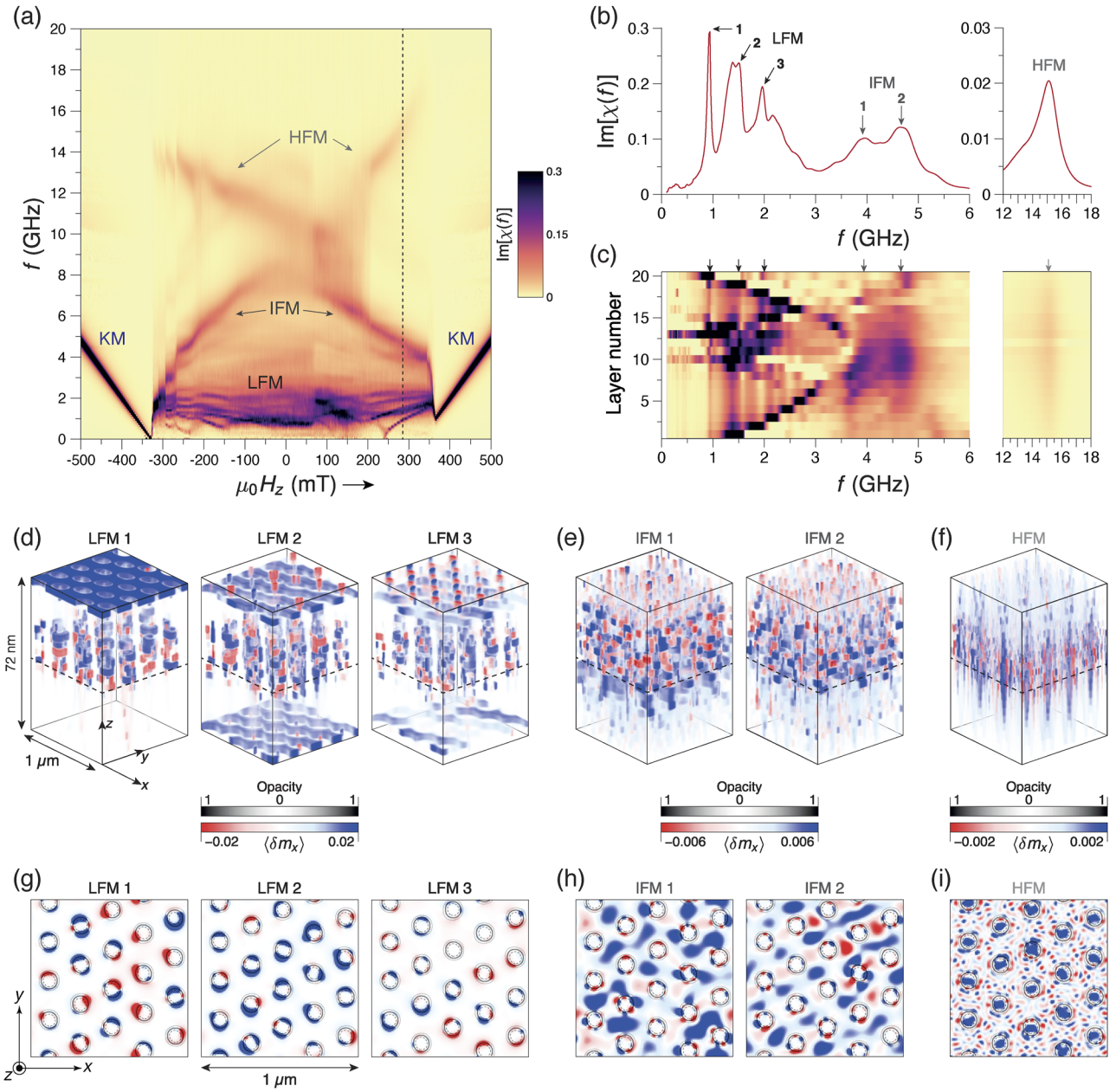

FIG. 4. Micromagnetic simulations of the dynamic response. (a) FMR spectra simulated by calculating the frequency-dependent susceptibility of multilayer to uniform excitation fields. (b) Imaginary part of the magnetic susceptibility at 285 mT [indicated by a dashed line in (a)], showing three LFM (0.94, 1.50, and 1.92 GHz), two IFM (3.90 and 4.24 GHz) and one HFM (15.10 GHz). (c) Thickness-resolved susceptibility at 285 mT. (d)–(f) Three-dimensional view of the magnetic response $\langle \delta m_x \rangle$ for (d) LFM, (e) IFM, and (f) HFM. (g)–(i) Two-dimensional view of the magnetic response $\langle \delta m_x \rangle$ in layer 10 of the modes in (d)–(f) for (g) LFM, (h) IFM, and (i) HFM.

in the range of positive magnetic fields $240 \leq \mu_0 H_z \leq 345$ mT, where a dense skyrmion lattice is stable. It then merges to a single IFM and then varies sharply until saturation. Several low frequency modes (LFMs), comprising several closely spaced branches in the frequency range of $0.5 < f < 2.5$ GHz, extend over the entire magnetic field range in which the magnetization is non-uniform. Finally, a high frequency mode (HFM) is also observed above 10 GHz with a positive field dispersion. It exhibits a sawtooth-like variation at negative fields and a smoother variation for positive fields. It is attenuated in the field range where magnetization profile consists of randomly oriented stripes [region (iv) in Fig. 3]. The simulated susceptibility map reproduces well the three families of modes observed experimentally

in the non-saturated state and gives good quantitative agreement for the mode frequencies. Note that in experiments, the LFM branches could not be resolved for the negative field side in the S_{21} transmission data of Fig. 2(a) (as opposed to the S_{11} and S_{22} reflection data, presented in Fig. 6 in the supplementary material). It is because these modes have a nearly flat frequency–field dispersion, and hence get diluted in the signal processing, which is necessary to remove the field independent offset. Only two of the LFM branches become resolvable when they acquire a certain slope on the positive field side, where the skyrmion density is constant and the skyrmion size strongly varies with the field.

The spatial profiles of the excited modes are found by driving the system at the mode frequencies identified in Fig. 4(a) and by recording the resonant response. In Fig. 4(b), we present the frequency response for $\mu_0 H_z = 285$ mT at which the equilibrium ground state is a skyrmion lattice, where we can identify well-defined peaks corresponding to the LFM, IFM, and HFM. Figure 4(c) gives layer-resolved susceptibility whose sum over all layers results in the curve in Fig. 4(b). For the LFM, we observe that the peaks in Fig. 4(b) correspond to two kinds of resonances. For LFM 1 at $f = 0.94$ GHz, the primary response arises from the central part of the stack in layers 13 and 14, and also from the top of the stack in layer 20. A similar behavior is seen for LFM 2 at 1.50 GHz, where layers 1 and 19, close to the stack surfaces, resonate along with the central part of the multilayer, as with LFM 3 at 1.92 GHz, where a strong response is seen in layers 2 and 18. This trend continues as the frequency increases, where successive layers farther away from the surfaces exhibit local resonances in conjunction with the central part. These mode profiles are visualized in Fig. 4(d), where we show the resonant fluctuations in the x component of the magnetization, $\langle \delta m_x \rangle$ (see Appendix D). Blue regions give the main response to the susceptibility, while the sum of equally intense blue and red regions cancel each other out. Similarly to Fig. 3(e), the opacity of the cells increase with the strength of the response in order to provide a clearer picture of their spatial profiles. LFM 1 mainly corresponds to the uniform precession of the background magnetization at the top of the multilayer stack, while the skyrmion edges are also excited in the central part of the stack with a small overall contribution to the susceptibility. This can be seen more clearly in Fig. 4(g), where the fluctuations are shown for layer 10. For LFM 2 and LFM 3, a similar behavior is seen where individual layers precess uniformly close to the surfaces, while excitations in the central part are localized to skyrmion edges.

For the IFM, two broad resonances are identified at $\mu_0 H_z = 285$ mT and correspond to excitations that are mainly localized to the central part of the multilayer [Figs. 4(c) and 4(e)]. The main contribution comes from the uniform precession of the background magnetization between the skyrmion cores, i.e., the inter-skyrmion region that is aligned parallel to the applied field, which can been seen from the predominantly blue regions in Fig. 4(h) that appear outside the cores. In addition, some SW channeling is also observed at the skyrmion edges, as shown by alternating red and blue patches encircling the skyrmions.

The HFM involves the in-phase precession of the reversed magnetization within the skyrmion cores and extends across most of the multilayer [Figs. 4(c) and 4(f)], with much of the power concentrated in the central part of the stack. The coherence of the precession can be seen in Fig. 4(i) by the uniform blue zones of $\langle \delta m_x \rangle$ within the $m_z = 0$ contours denoted by the continuous black circles. Moreover, this precession results in the generation of short wavelength SWs in the inter-skyrmion region, which are almost as intense as the core precession. However, only the volume occupied by the skyrmion cores provides a coherent response to the susceptibility for the HFM, which explains its much weaker intensity compared to the IFM and KM.

These features are also present at other applied field values at which the equilibrium state comprises nonuniform magnetization. (Fig. 7 in the supplementary material shows an analogous behavior at $\mu_0 H_z = -285$ mT, where the lattice possesses a lower skyrmion density with deformed core profiles.) At $\mu_0 H_z = 140$ mT, where the equilibrium state comprises labyrinthine domains, only the LFM and IFM are present, which further highlights the link between the HFM and the precessing skyrmion cores (Fig. 8 in the supplementary material). At zero field, the equilibrium state comprises a mixture of bubbles and elongated stripes in which no clear background orientation can be defined. Here, LFM persist while the IFM and HFM are absent. Instead, we can observe the existence of cavity modes that represent confined spin waves (Fig. 9 in the supplementary material).

E. Spin wave emission from the high frequency mode

The short wavelength SWs associated with the HFM cannot be excited directly with the uniform driving fields used in FMR, so their presence indicates the skyrmion cores act as nanoscale transducers that convert a spatially uniform drive into a spatially nonuniform excitation. To obtain deeper insight into this process, we focus on the HFM in the simulation data at two values of the applied fields, 300 and 364 mT, as presented in Fig. 5. The equilibrium state at 300 mT comprises a skyrmion lattice, with a skyrmion density of 20 μm^{-2} and an average core-to-core distance of $L = 262$ nm, while only one metastable skyrmion is present at 364 mT within the same area. The skyrmion diameters are roughly equivalent at these field values, which are 95 and 94 nm, respectively. The susceptibility at these two fields, shown in Fig. 5(a) for the range of 12–17 GHz, display a clear resonance peak around 15.5 GHz, which is over an order of magnitude larger at 300 mT than at 364 mT due to the difference in the skyrmion density.

At both field values, the coherent precession of the reversed magnetization within the skyrmion cores emit spin waves into the ferromagnetic background. Their wavelengths are similar at both fields and are estimated from the $\langle \delta m_x \rangle$ profiles in layer 10 shown in Figs. 5(b) and 5(c), yielding $\lambda \simeq 60$ nm and $\lambda \simeq 54$ nm at $\mu_0 H_z = 300$ mT and $\mu_0 H_z = 364$ mT, respectively. Despite the strong variations in the static core profile across the multilayer thickness, the emitted spin waves are remarkably coherent across the thickness. This can be seen in Fig. 5(d) for 300 mT and Fig. 5(e) for 364 mT where coherent wavefronts, driven in the central part of the multilayer at which the core diameter is greatest, extend across much of the multilayer thickness. The left inset in Figs. 5(d) and 5(e) indicate the number of topological charges per layer, which shows that the spin wave emission is just as effective for the topological bubbles residing primarily in the bottom of the stack as for the non-topological bubbles residing primarily in the top.

The overall coherence of these spin wave excitations can also be seen from the layer-averaged spatial discrete Fourier transform

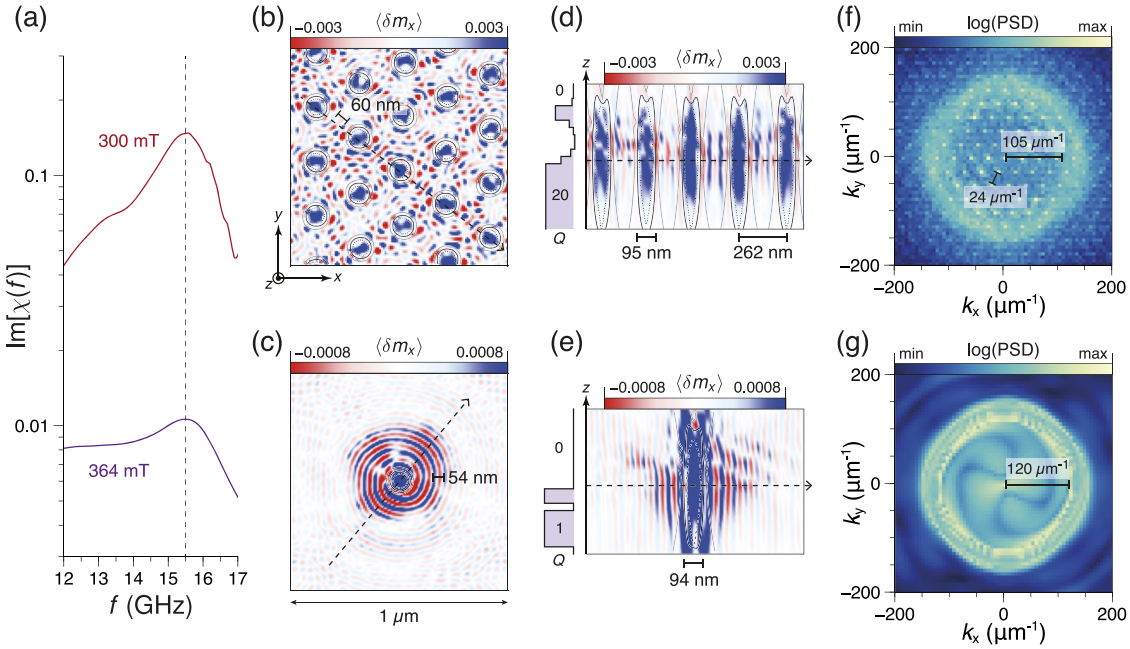

FIG. 5. Emission and interference of spin waves in skyrmion lattice. (a) Simulated susceptibility curves at 300 and 364 mT with the dynamic magnetization profiles $\langle \delta m_x \rangle$ in (b) and (c) of layer 10, respectively, corresponding to the resonance at 15.5 GHz. Cross sections of $\langle \delta m_x \rangle$ marked by dotted lines in (b) and (c) are also shown, respectively, in panels (d) and (e), highlighting the in-phase skyrmions core precession (in blue) and spin wave emission in the surrounding medium (alternate blue and red zones). (f) and (g) Power spectral density (PSD) of the layer averaged spatial discrete Fourier transform of the dynamic magnetization profiles indicating the average k_{SW}-vector of the emitted SWs at 300 and 364 mT, respectively. At 300 mT, the skyrmion lattice parameter can also be deduced from the $k = 24\ \mu\text{m}^{-1}$ periodic pattern seen in the spatial Fourier transform.

of the dynamical magnetization shown in Figs. 5(b) and 5(c). These Fourier maps, shown in Figs. 5(f) and 5(g), display a ring pattern with wave vectors $100 < k_{SW} < 150\ \mu\text{m}^{-1}$ corresponding to wavelengths $40 < \lambda < 60$ nm. At 300 mT, the pattern in the Fourier transformed data also manifests the periodic structure of the skyrmion lattice, from which the lattice periodicity can be estimated as shown in Fig. 5(f), using $2\pi/k = 262$ nm, where $k = 24\ \mu\text{m}^{-1}$.

The spin wave dynamics can be understood from the linearized equations of motion for the dynamic magnetization $\delta\mathbf{m}$, $\partial_t \delta\mathbf{m} = -|\gamma_0|(\delta\mathbf{m} \times \mathbf{H}_{\text{eff},0} + \mathbf{m}_0 \times \delta\mathbf{H}_{\text{eff}})$, where $\mathbf{m}_0$ is the static magnetization configuration and $\mathbf{H}_{\text{eff},0}$ is the static effective (internal) field associated with $\mathbf{m}_0$, while $\delta\mathbf{H}_{\text{eff}}$ is the dynamic effective (internal) field associated with $\delta\mathbf{m}$. The full 3D structure of the core and the surrounding configuration determines the spatial profile of the static internal field and the localization of the mode. The average value of this static internal field $\mathbf{H}_{\text{eff},0}(\mathbf{r})$ inside the skyrmion core can be extracted from micromagnetic simulations and is about −200 mT, which leads to resonances at 5.8 GHz without any confinement effects. To this, one needs to add the dynamic dipolar and exchange contributions $\delta\mathbf{H}_{\text{eff}}(\mathbf{r}, t)$ due to the localization of magnetization dynamics in a volume of $\sim 100 \times 100 \times 50\ \text{nm}^3$, which increases the resonant frequency to about 15 GHz (see Note 2 in the supplementary material). Similarly, we can estimate the wavelength of the emitted SWs by using the dispersion relation of forward-volume SWs in the inter-skyrmion region. At 300 mT, the average internal field in this region is around 110 mT, which results in a wavelength of 60 nm at 15.5 GHz, a group velocity of 960 m/s and an attenuation length of 490 nm (see Fig. 10 in the supplementary material). These estimations are in good agreement with the SW characteristics observed in Fig. 5.

The difference between the mode profiles shown in Figs. 5(b) and 5(c) is due to interference effects. At low skyrmion densities, the SW emitted at one core attenuates before reaching another, resulting in the familiar concentric ripples around each excitation source. At higher skyrmion densities, on the other hand, the inter-skyrmion distance is smaller than the attenuation length and interference patterns can arise. The cores can emit SWs in a broad spectral range, which depends on the excitation frequency and the skyrmion size (see Fig. 11 in the supplementary material). As such, the overall collective behavior is governed by a subtle interplay between the characteristic length scales of the system. The skyrmion diameter, which varies with the applied magnetic field, determines the precession frequency of the core thereby the wavelength of the emitted SWs, whereas constructive or destructive SW interference patterns are determined by the commensurability of SW wavelength and lattice parameters.

III. DISCUSSION

SW emission related to the HFM can have advantages over other reported methods of sub-100 nm wavelength generation. For example, magnetic vortex cores, which can act as SW emitters, require confined geometries such as dots for their existence and do not spontaneously form lattice structures in continuous films, which

precludes the appearance of SW interference phenomena seen here. The precession frequency of the skyrmions in our samples is also above the FMR gap of the surrounding domain background and hence SWs can be excited at this frequency in the same medium, unlike in other hybrid structures such as Pt/Co/YIG.[61] Moreover, the SWs generated in PMA materials are forward-volume SWs, which propagate isotropically[62] compared to backward-volume and Damon–Eshbach modes in in-plane magnetized systems, while maintaining high group velocities.

An interesting analogy of our skyrmion lattice as SW emitters can be made with arrays of spin–torque nano-oscillators, which can become synchronized by the generation and exchange of propagating SWs.[63] These structures have been proposed for implementing unconventional computing schemes.[5,64] We have shown here that SWs can be emitted in the uniform background by the skyrmion dynamics, but one also expects that in return, SWs can influence the skyrmion dynamics,[39] which could enlarge the processing capabilities of this type of devices.

Our study also paves the way toward creating reconfigurable magnonic crystals, since the skyrmion lattices we observe are quasi-periodic and dynamically tunable.[37] We can get a glimpse of the role of this lattice in the observation of SW interference patterns in the simulated HFM. However, the properties of the skyrmion lattice as a magnonic crystal also need to be explored using broadband propagating SW spectroscopy[10] or advanced SW imaging methods.[9,25] Finally, our system could serve as a platform to study magnon–skyrmion scattering,[39] emergent magnon motifs,[65] or chiral magnonic edge states.[66]

SUPPLEMENTARY MATERIAL

See the supplementary material for supporting information on the methodology and data related to the experimental and simulation work.

ACKNOWLEDGMENTS

The authors thank Sophie Collin for her assistance in the film growth. This work was partially supported by the Agence Nationale de la Recherche (ANR) under Grant No. ANR-17-CE24-0025 (TOPSKY) and the Horizon2020 Research Framework Program of the European Commission under Contract Nos. 824123 (SKYTOP) and 899646 (k-NET). It was also supported by a public grant overseen by the ANR as part of the "Investissements d'Avenir" program (Labex NanoSaclay, reference: ANR-10-LABX-0035).

AUTHOR DECLARATIONS

Conflict of Interest

The authors have no conflicts to disclose.

Author Contributions

Titiksha Srivastava: Formal analysis (equal); Investigation (equal); Methodology (equal); Software (supporting); Validation (equal); Visualization (equal); Writing – original draft (lead); Writing – review & editing (equal). **Yanis Sassi**: Resources (supporting). **Fernando Ajejas**: Resources (supporting). **Aymeric Vecchiola**: Resources (supporting). **Igor Ngouagnia Yemeli**: Resources (supporting). **Hervé Hurdequint**: Resources (supporting). **Karim Bouzehouane**: Resources (supporting). **Nicolas Reyren**: Conceptualization (equal); Funding acquisition (lead); Resources (supporting); Writing – review & editing (equal). **Vincent Cros**: Conceptualization (equal); Funding acquisition (supporting); Resources (lead); Writing – review & editing (equal). **Thibaut Devolder**: Formal analysis (equal); Methodology (equal); Resources (supporting); Writing – review & editing (equal). **Joo-Von Kim**: Conceptualization (equal); Formal analysis (equal); Funding acquisition (equal); Investigation (equal); Software (equal); Validation (equal); Visualization (equal); Writing – original draft (equal); Writing – review & editing (equal). **Grégoire de Loubens**: Conceptualization (equal); Formal analysis (equal); Funding acquisition (equal); Investigation (equal); Methodology (equal); Supervision (equal); Validation (equal); Visualization (equal); Writing – original draft (equal); Writing – review & editing (equal).

DATA AVAILABILITY

The data that support the findings of this study are available from the corresponding author upon reasonable request.

APPENDIX A: EXPERIMENTAL DETAILS

Ta(10)/Pt(8)/[FeCoB(1.2)/AlO$_x$(1.0)/Pt(1.6)]$_{19}$/FeCoB(1.2)/AlO$_x$(1.0)/Pt(3) multilayer stacks (where FeCoB ≡ $Fe_{70}Co_{10}B_{20}$, and thicknesses given in nm) were deposited by dc magnetron sputtering at room temperature on thermally oxidized silicon substrates, under Ar gas flow at a pressure of 0.25 Pa. The base pressure of the sputtering equipment was 5×10^{-6} Pa. magnetization cycles were measured by alternating gradient force magnetometry on 3×3 mm^2 films. MFM images were obtained at room temperature and ambient pressure using a double-pass lift mode, detecting the phase shift (MFM signal) of the second pass after a topographic measurement. The employed low moment tips were homemade.[49] Small permanent magnets with tunable gap and calibrated values of field were used to bias the samples while imaging them. VNA-FMR was conducted on 2×4 mm^2 films facing the 50 μm wide central conductor of a 50 Ω matched coplanar waveguide. The OP magnetic field was ramped up and down between −550 and +550 mT. For each of the 400 field steps, the VNA frequency was swept from 0.1 to 20 GHz with a number of points set to 1491 and a sweep time of 45 s. To improve the signal to noise ratio, the data were averaged over 30 magnetic field cycles. To remove the field independent background and normalize the transmission signal data S_{21}, we calculate $d_D S_{21}$ using the derivative divide method.[67] To increase the contrast further, we apply an additional frequency differentiation, and plot the imaginary part of the obtained quantity in Fig. 2(a).

APPENDIX B: EXTRACTION OF MAGNETIC PARAMETERS

The magnetization of the studied multilayers was determined by SQUID magnetometry. The 1.2 nm thick FeCoB is found to have a saturation magnetization $M_s = 1.20 \pm 0.1$ MA/m. Using angle

dependent cavity-FMR, the gyromagnetic ratio $\gamma_0/(2\pi) = 28.75 \pm 0.10$ GHz/T and the total uniaxial anisotropy field including demagnetizing and PMA contributions $\mu_0(M_s - H_k) = 354.7 \pm 0.5$ mT are determined (see Note 1 in the supplementary material). In the case of uniaxial anisotropy $\mu_0 H_k = 2K_u/M_s$; hence, $K_u = 0.69 \pm 0.11$ MJ/m^3. By assuming $M_s = 1.2$ MA/m and $K_u = 0.7$ MJ/m^3, the DMI and exchange parameters were iteratively determined by adjusting the period of the simulated labyrinthine domains to the one ($\simeq 170$ nm) observed by MFM at remanence.[49] We find the DMI constant to be $D = 1.2$ mJ/m^2 for an exchange constant $A = 15$ pJ/m.

APPENDIX C: DETERMINATION OF SKYRMION DIAMETER

From the MFM measurements of the quasi static magnetic configuration as a function of the applied field, we extract skyrmion density by using a MATLAB program that uses binarization. However, as the image resolution is not good enough to estimate the skyrmion diameters directly from the MFM images (which would anyway require to know the transfer function of the tip,[68] and might be complicated by the influence of the tip's stray field), we extract the apparent skyrmion diameters ($2R_{sk}$) indirectly, for the field values where the skyrmion density (d_{sk}) is close to maximum, using the out-of-plane experimental magnetization curve: $R_{sk} = \sqrt{(1 - m_z)/(2\pi d_{sk})}$. In Fig. 1(c), the error bars constitute the errors on the skyrmion density (proportional to the density and inversely proportional to the image size: ~8%) and magnetic field values to account for the slight misalignment of the magnetic pole and the magnetic tip in the MFM setup (10%). In the case of simulated MFM images, we used the same MATLAB program that binarizes the simulated MFM images, detects and finds the diameters of all the skyrmions, and calculates the mean and the standard deviation. For the simulations, we also compared the skyrmion diameter (i) calculated by the program and (ii) estimated from skyrmion density and m_z curve as a function of field when the skyrmion density is close to maximum. The small difference in the skyrmion diameters for the two methods lies within the standard deviation of the former method, indicated by the shaded area in gray in Fig. 3(b).

APPENDIX D: MICROMAGNETIC SIMULATIONS

Simulations were carried out with the open-source finite-difference micromagnetics code MUMAX3.[59] We used values of $M_s = 1.3375$ MA/m and $K_u = 0.9$ MJ/m^3, which are slightly larger than the experimentally determined values but were chosen to reproduce quantitatively the mode frequencies (see Fig. 12 in the supplementary material). The geometry consists of a rectangular slab of volume 1 μm × 1 μm × 72 nm discretized using 128 × 128 × 60 rectangular cells for the susceptibility calculations and a volume of 2 μm × 2 μm × 72 nm with 256 × 256 × 60 cells for the quasi-static hysteresis loop calculations. The simulated stack consists of 20 ferromagnetic layers with thickness 1.2 nm separated by 2.4 nm empty spacers, which accurately mimics the experimental stack, in which the total thickness of non-magnetic Pt and AlO_x layers separating adjacent FeCoB layers is 2.6 nm. Periodic boundary conditions are used in x and y directions in the film plane. The code performs a numerical time integration of the Landau–Lifshitz–Gilbert equation for the magnetization dynamics,

$$\frac{d\mathbf{m}}{dt} = -|\gamma_0|\mathbf{m} \times \mathbf{H}_{\text{eff}} + \alpha\mathbf{m} \times \frac{d\mathbf{m}}{dt}, \tag{D1}$$

where $\|\mathbf{m}(\mathbf{r}, t)\| = 1$ is a unit vector representing the orientation of the magnetization field, $\gamma_0 = \mu_0 g \mu_B/\hbar$ is the gyromagnetic constant, and α is the Gilbert damping constant. The effective field, $\mathbf{H}_{\text{eff}} = -(1/\mu_0 M_s)\delta U/\delta \mathbf{m}$, represents a variational derivative of the total magnetic energy U with respect to the magnetization, where U contains contributions from the Zeeman, nearest-neighbor Heisenberg exchange, interfacial Dzyaloshinskii–Moriya, and dipole–dipole interactions along with a uniaxial anisotropy with an easy axis along $\hat{\mathbf{z}}$, perpendicular to the film plane. Note that while the lateral cell size of 7.8125 nm used for the simulations presented here is larger than the characteristic exchange length, $l_{\text{ex}} = \sqrt{2A/\mu_0 M_s^2} \simeq 3.65$ nm, we have verified that using smaller discretization cells do not affect the salient features presented here (see Fig. 13 in the supplementary material).

To simulate quasi-static processes such as hysteresis loops, we begin with a uniform magnetic state oriented along $-z$ under an applied field of $\mu_0 H_z = -500$ mT. A Langevin-dynamics simulation with $T = 300$ K is then performed over 1 ns to mimic experimental conditions in which thermal fluctuations help to sample different metastable states in the energy landscape. The system is then relaxed without the precessional term in Eq. (D1) toward an energy minimum. This procedure of running Langevin dynamics, followed by relaxation, is then repeated two more times. After this, the micromagnetic configuration is recorded and assigned as the equilibrium state for the applied field value. This equilibrium state then serves as the initial state for the next value of the applied field, which is increased to $\mu_0 H_z = 500$ mT in increments of 1 mT. The simulated MFM images are computed from the equilibrium state by assuming a sample-to-tip distance of 50 nm.

To simulate the microwave susceptibility of the FeCoB multilayer, we compute the response of the magnetization to harmonic excitation fields. While it is common practice (and usually more efficient computationally) to calculate the eigenmode spectra from the Fourier transform of the transient response to pulsed fields, such an approach for the present system results in strong artifacts arising from non-resonant drift of the background magnetic state, such as the displacement of the skyrmion lattice or labyrinthine domain structure. Instead, we adopt an approach that more closely resembles the experimental protocol. For each value of the external field H_z, we compute the response of the precomputed static configuration, $m_0(\mathbf{r})$, to sinusoidal in-plane fields with frequency f, $h_x = h_{\text{rf}} \sin(2\pi f t)$, over 20 periods $\tau = 1/f$, where the spatial average of the resulting component $m_x(t)$ is recorded at intervals of 0.1 τ. In this procedure, the Gilbert damping parameter is set to $\alpha = 0.02$ and the excitation amplitude to $\mu_0 h_{\text{rf}} = 0.1$ mT (1 mT in Figs. 12 and 13 in the supplementary material). We estimate the imaginary part of the susceptibility χ at this frequency, $\text{Im}[\chi(f)]$, by projecting $\langle m_x(t)\rangle$ onto $-\cos(2\pi f t)$,

$$\text{Im}[\chi(f)] \simeq -\frac{1}{20\tau}\int_0^{20\tau} \langle m_x(t)\rangle \cos(2\pi f t)\, dt, \tag{D2}$$

which is the quantity shown in Figs. 4(a) and 4(b). $\mathrm{Im}[\chi(f)]$ exhibits peaks at resonance when m_x is in perfect quadrature with respect to h_x. This procedure is repeated as a function of f ranging from 0.1 to 20 GHz in steps of 0.1 GHz for the map in Fig. 4(a) and in steps of 0.02 GHz for the data in Figs. 4(b) and 4(c).

The spatial mode profile at a given mode resonance f_n is extracted by driving the system harmonically at f_n with $h_x = h_{\mathrm{rf}} \sin(2\pi f_n t)$ and by recording, cell-by-cell, the components of magnetization at intervals of 0.1 τ_n, as for the calculation of the susceptibility. The mode profiles are characterized by the fluctuation amplitude $\langle \delta m_x(\mathbf{r}) \rangle$, which is computed in an analogous way to the susceptibility, where we drive the system over 100 periods and then compute, after transients are washed out,

$$\langle \delta m_x(\mathbf{r}) \rangle = -\frac{1}{2\tau_n} \int_0^{2\tau_n} [m_x(\mathbf{r}, t) - m_{x,0}(\mathbf{r})] \cos(2\pi f_n t) dt, \quad \text{(D3)}$$

over two additional periods. Visually, dark blue regions contribute most to the overall $\mathrm{Im}[\chi(f)]$, while equally dark red and blue regions cancel each other out because they represent fluctuations with opposite sign.

REFERENCES

[1] V. V. Kruglyak, S. O. Demokritov, and D. Grundler, "Magnonics," J. Phys. D: Appl. Phys. **43**, 264001 (2010).
[2] M. Krawczyk and D. Grundler, "Review and prospects of magnonic crystals and devices with reprogrammable band structure," J. Condens. Matter Phys. **26**, 123202 (2014).
[3] A. Barman, G. Gubbiotti, S. Ladak, A. O. Adeyeye, M. Krawczyk, J. Gräfe, C. Adelmann, S. Cotofana, A. Naeemi, V. I. Vasyuchka *et al.*, "The 2021 magnonics roadmap," J. Phys.: Condens. Matter **33**, 413001 (2021).
[4] G. Csaba, Á. Papp, and W. Porod, "Perspectives of using spin waves for computing and signal processing," Phys. Lett. A **381**, 1471–1476 (2017).
[5] F. Macià, A. D. Kent, and F. C. Hoppensteadt, "Spin-wave interference patterns created by spin-torque nano-oscillators for memory and computation," Nanotechnology **22**, 095301 (2011).
[6] Á. Papp, W. Porod, Á. I. Csurgay, and G. Csaba, "Nanoscale spectrum analyzer based on spin-wave interference," Sci. Rep. **7**, 9245 (2017).
[7] A. V. Chumak, A. A. Serga, and B. Hillebrands, "Magnon transistor for all-magnon data processing," Nat. Commun. **5**, 4700 (2014).
[8] M. Grassi, M. Geilen, D. Louis, M. Mohseni, T. Brächer, M. Hehn, D. Stoeffler, M. Bailleul, P. Pirro, and Y. Henry, "Slow-wave-based nanomagnonic diode," Phys. Rev. Appl. **14**, 024047 (2020).
[9] H. Merbouche, M. Collet, M. Evelt, V. E. Demidov, J. L. Prieto, M. Muñoz, J. Ben Youssef, G. de Loubens, O. Klein, S. Xavier *et al.*, "Frequency filtering with a magnonic crystal based on nanometer-thick yttrium iron garnet films," ACS Appl. Nano Mater. **4**, 121–128 (2021).
[10] F. Ciubotaru, T. Devolder, M. Manfrini, C. Adelmann, and I. P. Radu, "All electrical propagating spin wave spectroscopy with broadband wavevector capability," Appl. Phys. Lett. **109**, 012403 (2016).
[11] H. Yu, G. Duerr, R. Huber, M. Bahr, T. Schwarze, F. Brandl, and D. Grundler, "Omnidirectional spin-wave nanograting coupler," Nat. Commun. **4**, 2702 (2013).
[12] H. Yu, O. d' Allivy Kelly, V. Cros, R. Bernard, P. Bortolotti, A. Anane, F. Brandl, F. Heimbach, and D. Grundler, "Approaching soft x-ray wavelengths in nanomagnet-based microwave technology," Nat. Commun. **7**, 11255 (2016).
[13] J. Chen, T. Yu, C. Liu, T. Liu, M. Madami, K. Shen, J. Zhang, S. Tu, M. S. Alam, K. Xia *et al.*, "Excitation of unidirectional exchange spin waves by a nanoscale magnetic grating," Phys. Rev. B **100**, 104427 (2019).
[14] H. Fulara, M. Zahedinejad, R. Khymyn, A. A. Awad, S. Muralidhar, M. Dvornik, and J. Åkerman, "Spin-orbit torque-driven propagating spin waves," Sci. Adv. **5**, eaax8467 (2019).
[15] H. Yu, J. Xiao, and H. Schultheiss, "Magnetic texture based magnonics," Phys. Rep. **905**, 1–59 (2021).
[16] B. E. Argyle, W. Jantz, and J. C. Slonczewski, "Wall oscillations of domain lattices in underdamped garnet films," J. Appl. Phys. **54**, 3370–3386 (1983).
[17] S. A. Montoya, S. Couture, J. J. Chess, J. C. T. Lee, N. Kent, M.-Y. Im, S. D. Kevan, P. Fischer, B. J. McMorran, S. Roy, V. Lomakin, and E. E. Fullerton, "Resonant properties of dipole skyrmions in amorphous Fe/Gd multilayers," Phys. Rev. B **95**, 224405 (2017).
[18] N. Vukadinovic, M. Labrune, J. B. Youssef, A. Marty, J. C. Toussaint, and H. Le Gall, "Ferromagnetic resonance spectra in a weak stripe domain structure," Phys. Rev. B **65**, 054403 (2001).
[19] U. Ebels, L. Buda, K. Ounadjela, and P. E. Wigen, "Ferromagnetic resonance excitation of two-dimensional wall structures in magnetic stripe domains," Phys. Rev. B **63**, 174437 (2001).
[20] G. Gubbiotti, G. Carlotti, S. Tacchi, M. Madami, T. Ono, T. Koyama, D. Chiba, F. Casoli, and M. G. Pini, "Spin waves in perpendicularly magnetized Co/Ni(111) multilayers in the presence of magnetic domains," Phys. Rev. B **86**, 014401 (2012).
[21] M. Buess, R. Höllinger, T. Haug, K. Perzlmaier, U. Krey, D. Pescia, M. R. Scheinfein, D. Weiss, and C. H. Back, "Fourier transform imaging of spin vortex eigenmodes," Phys. Rev. Lett. **93**, 077207 (2004).
[22] V. Castel, J. Ben Youssef, F. Boust, R. Weil, B. Pigeau, G. de Loubens, V. V. Naletov, O. Klein, and N. Vukadinovic, "Perpendicular ferromagnetic resonance in soft cylindrical elements: Vortex and saturated states," Phys. Rev. B **85**, 184419 (2012).
[23] F. Garcia-Sanchez, P. Borys, R. Soucaille, J.-P. Adam, R. L. Stamps, and J.-V. Kim, "Narrow magnonic waveguides based on domain walls," Phys. Rev. Lett. **114**, 247206 (2015).
[24] K. Wagner, A. Kákay, K. Schultheiss, A. Henschke, T. Sebastian, and H. Schultheiss, "Magnetic domain walls as reconfigurable spin-wave nanochannels," Nat. Nanotechnol. **11**, 432–436 (2016).
[25] S. Wintz, V. Tiberkevich, M. Weigand, J. Raabe, J. Lindner, A. Erbe, A. Slavin, and J. Fassbender, "Magnetic vortex cores as tunable spin-wave emitters," Nat. Nanotechnol. **11**, 948–953 (2016).
[26] G. Dieterle, J. Förster, H. Stoll, A. S. Semisalova, S. Finizio, A. Gangwar, M. Weigand, M. Noske, M. Fähnle, I. Bykova, J. Gräfe *et al.*, "Coherent excitation of heterosymmetric spin waves with ultrashort wavelengths," Phys. Rev. Lett. **122**, 117202 (2019).
[27] A. Fert, N. Reyren, and V. Cros, "Magnetic skyrmions: Advances in physics and potential applications," Nat. Rev. Mater. **2**, 17031 (2017).
[28] C. Moreau-Luchaire, C. Moutafis, N. Reyren, J. Sampaio, C. A. F. Vaz, N. Van Horne, K. Bouzehouane, K. Garcia, C. Deranlot, P. Warnicke *et al.*, "Additive interfacial chiral interaction in multilayers for stabilization of small individual skyrmions at room temperature," Nat. Nanotech **11**, 444–448 (2016).
[29] O. Boulle, J. Vogel, H. Yang, S. Pizzini, D. de Souza Chaves, A. Locatelli, T. O. M. A. Sala, L. D. Buda-Prejbeanu, O. Klein, M. Belmeguenai *et al.*, "Room temperature chiral magnetic skyrmion in ultrathin magnetic nanostructures," Nat. Nanotechnol. **11**, 449–454 (2016).
[30] T. Srivastava, M. Schott, R. Juge, V. Křižáková, M. Belmeguenai, Y. Roussigné, A. Bernand-Mantel, L. Ranno, S. Pizzini, S.-M. Chérif *et al.*, "Large-voltage tuning of Dzyaloshinskii–Moriya interactions: A route toward dynamic control of skyrmion chirality," Nano Lett. **18**, 4871–4877 (2018).
[31] W. Jiang, P. Upadhyaya, W. Zhang, G. Yu, M. B. Jungfleisch, F. Y. Fradin, J. E. Pearson, Y. Tserkovnyak, K. L. Wang, O. Heinonen, S. G. E. te Velthuis, and A. Hoffmann, "Blowing magnetic skyrmion bubbles," Science **349**, 283–286 (2015).
[32] S. Woo, K. Litzius, B. Krüger, M.-Y. Im, L. Caretta, K. Richter, M. Mann, A. Krone, R. M. Reeve, M. Weigand *et al.*, "Observation of room-temperature magnetic skyrmions and their current-driven dynamics in ultrathin metallic ferromagnets," Nat. Mater. **15**, 501–506 (2016).
[33] F. Garcia-Sanchez, J. Sampaio, N. Reyren, V. Cros, and J.-V. Kim, "A skyrmion-based spin-torque nano-oscillator," New J. Phys. **18**, 075011 (2016).
[34] G. Finocchio, M. Ricci, R. Tomasello, A. Giordano, M. Lanuzza, V. Puliafito, P. Burrascano, B. Azzerboni, and M. Carpentieri, "Skyrmion based microwave detectors and harvesting," Appl. Phys. Lett. **107**, 262401 (2015).
[35] F. Ma, Y. Zhou, H. B. Braun, and W. S. Lew, "Skyrmion-based dynamic magnonic crystal," Nano Lett. **15**, 4029–4036 (2015).

[36]M. Mruczkiewicz, P. Gruszecki, M. Zelent, and M. Krawczyk, "Collective dynamical skyrmion excitations in a magnonic crystal," Phys. Rev. B **93**, 174429 (2016).
[37]M. Garst, J. Waizner, and D. Grundler, "Collective spin excitations of helices and magnetic skyrmions: Review and perspectives of magnonics in non-centrosymmetric magnets," J. Phys. D: Appl. Phys. **50**, 293002 (2017).
[38]X.-g. Wang, Y.-Z. Nie, Q.-l. Xia, and G.-h. Guo, "Dynamically reconfigurable magnonic crystal composed of artificial magnetic skyrmion lattice," J. Appl. Phys. **128**, 063901 (2020).
[39]C. Schütte and M. Garst, "Magnon-skyrmion scattering in chiral magnets," Phys. Rev. B **90**, 094423 (2014).
[40]J.-V. Kim, F. Garcia-Sanchez, J. Sampaio, C. Moreau-Luchaire, V. Cros, and A. Fert, "Breathing modes of confined skyrmions in ultrathin magnetic dots," Phys. Rev. B **90**, 064410 (2014).
[41]V. L. Zhang, C. G. Hou, K. Di, H. S. Lim, S. C. Ng, S. D. Pollard, H. Yang, and M. H. Kuok, "Eigenmodes of Néel skyrmions in ultrathin magnetic films," AIP Adv. **7**, 055212 (2017).
[42]M. Mruczkiewicz, M. Krawczyk, and K. Y. Guslienko, "Spin excitation spectrum in a magnetic nanodot with continuous transitions between the vortex, Bloch-type skyrmion, and Néel-type skyrmion states," Phys. Rev. B **95**, 094414 (2017).
[43]V. P. Kravchuk, D. D. Sheka, U. K. Rößler, J. van den Brink, and Y. Gaididei, "Spin eigenmodes of magnetic skyrmions and the problem of the effective skyrmion mass," Phys. Rev. B **97**, 064403 (2018).
[44]Y. Onose, Y. Okamura, S. Seki, S. Ishiwata, and Y. Tokura, "Observation of magnetic excitations of skyrmion crystal in a helimagnetic insulator Cu_2OSeO_3," Phys. Rev. Lett. **109**, 037603 (2012).
[45]T. Schwarze, J. Waizner, M. Garst, A. Bauer, I. Stasinopoulos, H. Berger, C. Pfleiderer, and D. Grundler, "Universal helimagnon and skyrmion excitations in metallic, semiconducting and insulating chiral magnets," Nat. Mater. **14**, 478–483 (2015).
[46]A. Aqeel, J. Sahliger, T. Taniguchi, S. Mändl, D. Mettus, H. Berger, A. Bauer, M. Garst, C. Pfleiderer, and C. H. Back, "Microwave spectroscopy of the low-temperature skyrmion state in Cu_2OSeO_3," Phys. Rev. Lett. **126**, 017202 (2021).
[47]B. Satywali, V. P. Kravchuk, L. Pan, M. Raju, S. He, F. Ma, A. P. Petrović, M. Garst, and C. Panagopoulos, "Microwave resonances of magnetic skyrmions in thin film multilayers," Nat. Commun. **12**, 1909 (2021).
[48]L. Flacke, V. Ahrens, S. Mendisch, L. Körber, T. Böttcher, E. Meidinger, M. Yaqoob, M. Müller, L. Liensberger, A. Kákay, M. Becherer, P. Pirro, M. Althammer, S. Geprägs, H. Huebl, R. Gross, and M. Weiler, "Robust formation of nanoscale magnetic skyrmions in easy-plane anisotropy thin film multilayers with low damping," Phys. Rev. B **104**, L100417 (2021).
[49]W. Legrand, J.-Y. Chauleau, D. Maccariello, N. Reyren, S. Collin, K. Bouzehouane, N. Jaouen, V. Cros, and A. Fert, "Hybrid chiral domain walls and skyrmions in magnetic multilayers," Sci. Adv. **4**, eaat0415 (2018).
[50]A. S. Savchenko, V. M. Kuchkin, F. N. Rybakov, S. Blügel, and N. S. Kiselev, "Chiral standing spin waves in skyrmion lattice," APL Mater. **10**, 071111 (2022).
[51]H. Yang, O. Boulle, V. Cros, A. Fert, and M. Chshiev, "Controlling Dzyaloshinskii–Moriya interaction via chirality dependent atomic-layer stacking, insulator capping and electric field," Sci. Rep. **8**, 12356 (2018).
[52]N.-H. Kim, J. Cho, J. Jung, D.-S. Han, Y. Yin, J.-S. Kim, H. J. M. Swagten, K. Lee, M.-H. Jung, and C.-Y. You, "Role of top and bottom interfaces of a Pt/Co/AlOx system in Dzyaloshinskii–Moriya interaction, interface perpendicular magnetic anisotropy, and magneto-optical Kerr effect," AIP Adv. **7**, 035213 (2017).
[53]S. Tacchi, R. E. Troncoso, M. Ahlberg, G. Gubbiotti, M. Madami, J. Åkerman, and P. Landeros, "Interfacial Dzyaloshinskii–Moriya interaction in Pt/CoFeB films: Effect of the heavy-metal thickness," Phys. Rev. Lett. **118**, 147201 (2017).
[54]Y. Ou, D. C. Ralph, and R. A. Buhrman, "Strong perpendicular magnetic anisotropy energy density at Fe alloy/HfO_2 interfaces," Appl. Phys. Lett. **110**, 192403 (2017).
[55]W. Legrand, Y. Sassi, F. Ajejas, S. Collin, L. Bocher, H. Jia, M. Hoffmann, B. Zimmermann, S. Blügel, N. Reyren, V. Cros, and A. Thiaville, "Spatial extent of the Dzyaloshinskii–Moriya interaction at metallic interfaces," Phys. Rev. Mater. **6**, 024408 (2022).
[56]M. Belmeguenai, M. S. Gabor, F. Zighem, N. Challab, T. Petrisor, R. B. Mos, and C. Tiusan, "Ferromagnetic-resonance-induced spin pumping in $Co_{20}Fe_{60}B_{20}$/Pt systems: Damping investigation," J. Phys. D: Appl. Phys. **51**, 045002 (2018).
[57]T. Böttcher, K. Lee, F. Heussner, S. Jaiswal, G. Jakob, M. Kläui, B. Hillebrands, T. Brächer, and P. Pirro, "Heisenberg exchange and Dzyaloshinskii–Moriya interaction in ultrathin Pt(W)/CoFeB single and multilayers," IEEE Trans. Magn. **57**, 1600207 (2021).
[58]H. Puszkarski, "Theory of interface magnons in magnetic multilayer films," Surf. Sci. Rep. **20**, 45–110 (1994).
[59]A. Vansteenkiste, J. Leliaert, M. Dvornik, M. Helsen, F. Garcia-Sanchez, and B. Van Waeyenberge, "The design and verification of MuMax3," AIP Adv. **4**, 107133 (2014).
[60]W. Li, I. Bykova, S. Zhang, G. Yu, R. Tomasello, M. Carpentieri, Y. Liu, Y. Guang, J. Gräfe, M. Weigand, D. M. Burn, G. der Laan, T. Hesjedal, Z. Yan, J. Feng, C. Wan, J. Wei, X. Wang, X. Zhang, H. Xu, C. Guo, H. Wei, G. Finocchio, X. Han, and G. Schütz, "Anatomy of skyrmionic textures in magnetic multilayers," Adv. Mater. **31**, 1807683 (2019).
[61]J. Chen, J. Hu, and H. Yu, "Chiral emission of exchange spin waves by magnetic skyrmions," ACS Nano **15**, 4372–4379 (2021).
[62]M. Sushruth, M. Grassi, K. Ait-Oukaci, D. Stoeffler, Y. Henry, D. Lacour, M. Hehn, U. Bhaskar, M. Bailleul, T. Devolder, and J.-P. Adam, "Electrical spectroscopy of forward volume spin waves in perpendicularly magnetized materials," Phys. Rev. Res. **2**, 043203 (2020).
[63]S. Sani, J. Persson, S. M. Mohseni, Y. Pogoryelov, P. K. Muduli, A. Eklund, G. Malm, M. Käll, A. Dmitriev, and J. Åkerman, "Mutually synchronized bottom-up multi-nanocontact spin–torque oscillators," Nat. Commun. **4**, 2731 (2013).
[64]M.-K. Lee and M. Mochizuki, "Reservoir computing with spin waves in a skyrmion crystal," Phys. Rev. Appl. **18**, 014074 (2022).
[65]S. Watanabe, V. S. Bhat, K. Baumgaertl, and D. Grundler, "Direct observation of worm-like nanochannels and emergent magnon motifs in artificial ferromagnetic quasicrystals," Adv. Funct. Mater. **30**, 2001388 (2020).
[66]S. A. Díaz, T. Hirosawa, J. Klinovaja, and D. Loss, "Chiral magnonic edge states in ferromagnetic skyrmion crystals controlled by magnetic fields," Phys. Rev. Res. **2**, 013231 (2020).
[67]H. Maier-Flaig, S. T. B. Goennenwein, R. Ohshima, M. Shiraishi, R. Gross, H. Huebl, and M. Weiler, "Note: Derivative divide, a method for the analysis of broadband ferromagnetic resonance in the frequency domain," Rev. Sci. Instrum. **89**, 076101 (2018).
[68]Y. Feng, P. M. Vaghefi, S. Vranjkovic, M. Penedo, P. Kappenberger, J. Schwenk, X. Zhao, A.-O. Mandru, and H. J. Hug, "Magnetic force microscopy contrast formation and field sensitivity," J. Magn. Magn. Mater. **551**, 169073 (2022).